Journal of Innovative Image Processing (ISSN: 2582-4252)
www.irojournals.com/iroiip/

Adaptive Linear Combination-Based Contrast-Preserving Decolourization of Macroscopic Skin Images

Sathish S.[1], Vinurajkumar S.[2], Babu G.[3], Praveen Kumar R.[4]

[1]Assistant Professor, [3]Professor, Department of Biomedical Engineering, Easwari Engineering College, Chennai, India.

[2]Assistant Professor, Department of Biomedical Engineering, SRM Institute of Science and Technology Ramapuram Campus, Chennai, India.

[4]Associate Professor, Department of ECE, Easwari Engineering College, Ramapuram, Chennai, India.

E-mail: [1]sathishdir@gmail.com, [2]rajkumar.vinu@gmail.com, [3]babutry@gmail.com, [4]rpjcspraveen@gmail.com

Abstract

The dermatological macro-images are colour images. The majority of the available image segmentation and feature extraction algorithms are designed for grayscale images. Hence, the conversion of dermatological images to grayscale is an important step in their automated analysis. Customized algorithms for decolourizing dermatological images are not available. The existing decolourization algorithms for natural-scene images focus only on the preservation of local contrast. Such algorithms may not ensure good accuracy of lesion segmentation on macroscopic images when intensity-based schemes are adopted. Decolourization algorithms that enable effective preservation of both gradient and intensity information are more desirable. This approach in especially, resulted in a 6–8% average DSC improvement over baselines, a 12% increase in the contrast index, and a 9% increase in the perceptual similarity score.

Keywords: Decolourization, Macroscopy Images, Segmentation Threshold, Skin Lesions.

1. Introduction

Photo-macrography or macro-photography provides a close-up view of skin lesions. The term ‘macroscopic image’ or ‘micro-image’ refers to a highly zoomed view of the lesions captured with the help of a microscope, as done in dermoscopy. [1] Because of the simplicity, flexibility, and availability of high-resolution digital cameras, dermatological photo-macrography is widely used in dermatology. Recently, [2,3] studies have proven the potential of wide-field dermatological photo-macrographs as tools for identifying the type of suspicious skin lesions at the pre-screening level. The potential of dermatological photo-macrography to detect melanoma has already been evidenced by many researchers [4]. They have demonstrated that an SVM classifier, which uses textural, intensity, and shape features of the lesion as input, can distinguish melanoma and nevus lesions with higher accuracy on dermatological photo-macrographs (98.06%) than on dermoscopy images (93.95%). Usually, the aggressiveness of a skin lesion, especially the possibility of it being malignant, is characterized by features such as the sharpness of the boundary (well-defined or ill-defined), continuity of the border, and

DOI: https://doi.org/10.36548/jiip.2025.3.015
Received: 12.07.2025, received in revised form: 15.07.2025, accepted: 03.09.2025, published: 16.09.2025

geometric/shape features like area, solidity, eccentricity, etc. The type and amount of texture and distinct structures present in the lesion area, along with intensity features within the lesion, are also often used. Consequently, the diagnosis of skin lesions greatly depends on the accurate segmentation of the lesions. Manual delineation of any lesion is highly subjective. A disagreement of 10-20% in the area of skin lesions delineated from dermoscopy images has been reported among expert dermatologists. In a similar study, an average disagreement of 15.28% in the area of skin lesions was found. In 10% of the dermoscopy images, the disagreement was reported to be above 28%. Reproducibility is lower in manual contouring, and automated methods have lower pixel misclassification compared to manual contouring. Automated segmentation algorithms are necessary to eliminate the inter-operator variability inherent in the subjective contouring of skin lesions. The segmentation process is inevitable in deep learning models used to characterize skin lesions from images. [5] Deep learning models can improve performance when localized lesions are used for training. InceptionResNetV2 improves the accuracy of detecting melanoma by 2.18% when segmented lesions are used for training instead of raw input images. In addition to the improvement in accuracy, the use of segmented lesions as input substantially reduces the time taken for training and inference. Even in deep learning models, the preprocessing and segmentation of lesions play a significant role in the accurate detection of melanoma (Adegun & Viriri 2021). The majority of available image segmentation and feature extraction algorithms are designed for grayscale images. However, dermatological macro-images are color images. Hence, converting dermatological images to grayscale is an important step in their automated analysis [6]. For example, the Local Binary Pattern-based Clustering (LBPC) operates on grayscale images. Color dermoscopy images are converted to grayscale before applying the LBPC. Similarly, the detection of edges of skin lesions is an intermediate step in the Delaunay Triangulation-based segmentation of skin lesions. [6] In this scheme, dermoscopy images are converted to grayscale before applying the Canny edge detection algorithm. In the fuzzy-based framework for detecting disease-induced color pigment networks, [7] dermoscopy images are converted to grayscale for extracting textural features. Our method adaptively optimizes weights based on both intensity and gradient preservation, which differs from previous fixed-weight or heuristic methods. This ensures that performance is consistent across different dermatological images.

Only the traditional model so far been adopted in literature to decolourize the macroscopic images of skin lesions. For converting the colour image to grayscale, [6] adopted the model Y= 0.2989 R + 0.5870 G + 0.1140 B. For conversion, by [7] adopted the model (Y = (R + G + B)/3).

2. Literature Review

In addition to the traditional models adopted in the literature to decolorize the macroscopic images of skin lesions, there are some decolorization algorithms in the literature. They are Correlation-based Decolorization (CD) (Nafchi et al. 2017), [8] Decolorization via Variance Maximization (DVM) (Jin et al. 2014), Fast Contrast Enhancing Decolorization (FCED) (Grundland & Dodgson, 2007), Semi-parametric Decolorization (SD) (Liu et al. 2017), Gradient Correlation Similarity-based Decolorization (GCSD) (Liu et al. 2015), and Log-Euclidean-based Decolorization (LED) [9,10].

In the CD (Nafchi et al. 2017), a contrast image is derived first. The intensity value at a particular location in the contrast image is computed from the product of the mean intensity of three color channels and standard deviation at that location. The decolorized image is computed

from a linear combination of the red, green, and blue color channels. The global weights corresponding to each channel are set proportional to the correlation of that channel with the contrast image.

In the DVM (Jin et al. 2014), an energy functional is used to determine the local values of the weights in the combination of red, green, and blue color channels. Minimizing the energy functional accounts for maximizing the variance with a constraint of minimum brightness error. To ensure piecewise smoothness and restrict noisiness by minimizing the differences among computed gray scale values in the decolorized image at nearby pixel locations, a total variation regularization term of the combination function is also included in the energy functional.

In the FCED [10], for finding the color axis that predominantly accounts for the diminished chromatic contrast caused by the inclusion of the luminance channel in the mapping process pertaining to the decolorization, a custom dimensionality reduction technique named predominant component analysis was used. The values in the predominant chromatic channel are produced by projecting the chromatic channel values onto the predominant chromatic axis. After that, the main chromatic channel is combined with the luminance channel, and the dynamic range of the new luminance channel is changed so that noise doesn't get louder. Based on the content of the saturation channel, the lower and upper bounds of the local values within the luminance channel that offer the desired contrast are estimated. Finally, the local intensity in the decolorized image is the median of corresponding values in the range-adjusted enhanced luminosity channel and matrices of lower and upper bounds of the local values within the luminance channel computed as per the contrast enhancement criteria.

In the SD (Liu et al. 2017), a second-degree polynomial given in (1.1) is used to compute the decolourized image 'I_o' from the red 'R_i', green 'G_i', and blue 'B_i' colour channels of the input colour image 'I_i'.

$$I_o = [W_1R_i + W_2G_i + W_3B_i] + [W_4R_iG_i + W_5R_iB_i + W_6G_iB_i] + [W_7(R_i)^2 + W_8(G_i)^2 + W_9(B_i)^2] \quad (1)$$

The SD is only semi-optimized because the weights '$W1$', '$W2$', and '$W3$' in (1) are set manually. Other weights '$W4$', '$W5$', '$W6$', '$W7$', '$W8$', and '$W9$' are computed iteratively by minimizing a bimodal objective function (the sum of two Gaussian terms) that accounts for contrast preservation. In the GCSD, the second degree polynomial used in the SD is also adopted to compute the decolourized image from the red, green, and blue colour channels. Weights of the polynomial model are estimated through iterative minimization of a loss function named gradient correlation similarity measure with the help of a combination of alternating direction and augmented Lagrangian methods. The loss function reflects the cumulative similarity between the gradient magnitudes in the decolourized image and those in the individual colour channels in a pixel-wise sense. [11,12]

In the LED (Liu et al. 2017), [13,14] the weights of the first-degree polynomial decolourization model that decide the relative significance of individual colour channels are considered as those values at which a log-Euclidean metric between gradients of the channels of input colour image and decolourized image is at its minimum. A limited number of candidate weight values within the interval [0 1] are considered and the candidate values at which the penalty function is minimum are identified.

Most of the decolourization algorithms in literature are designed and validated on natural-scene images. Customized algorithms for decolourizing dermatological images are not

available. There are extensive studies that evaluate the performance of decolourization algorithms in contexts like document binarization (Hedjam et al. 2015) and face recognition (Kanan & Cottrell 2012). Similar studies on dermatological images are not available. The existing decolourization algorithms CD, DVM, FCED, SD, GCSD, and LED (Liu et al. 2017) focus only on the preservation of local contrast or gradient magnitude. Such algorithms may not ensure good accuracy of lesion segmentation on macroscopic images when intensity-based schemes are adopted. Hence, a decolourization algorithm that enables effective preservation of both gradient and intensity information is more desirable.

To address these issues, a novel decolourization algorithm named Adaptive Linear Combination-based Contrast-preserving Decolourization (ALCCD) that preserves the contrast between the lesion and background skin regions when mapped from colour space to greyscale space and ensures accurate segmentation is proposed.

3. Materials and Methods

To fill these gaps, a decolourization algorithm named Adaptive Linear Combination-based Contrast-preserving Decolourization (ALCCD) that preserves the contrast between the background skin regions, and the lesion when mapped from colour space to grey scale space and ensures accurate segmentation is proposed. Test Dataset: The dermatological photographs used in this thesis are downloaded from the 'DermQuest [7] data repository. The DermQuest database is owned by the Vision and Image Processing Laboratory, University of Waterloo, Canada. A total of 137 images are used in this thesis. Among the 137 macroscopic images 61 images are nevus and 76 images are melanoma cases.

The Flow of the work is termed as such follows 1. Preprocessing, 2. Adaptive weight optimization, 3. Grayscale conversion, and 4. Segmentation evaluation steps.

4. Proposed Work

In the ALCCD, the RGB vector '$X(m, n) = \{X_R(m, n), X_G(m, n), X_B(m, n)\}$' in the colour image '$X$' at an arbitrary location '(m, n), $m = 1,2, \dots \dots, M$ & $n = 1,2, \dots \dots, N$' is converted to grey scale value '$Y(m, n)$' via a simple linear combination as shown in (2).

$$Y(m,n) = \varphi\big(X(m,n)\big) = W_R(m,n)X_R(m,n) + W_G(m,n)X_G(m,n) + W_B(m,n)X_B(m,n) \quad (2)$$

The algebraic form of the mapping function 'φ' that describe the decolourization process is,

$$\begin{aligned} Y(m,n) = \varphi\big(X(m,n)\big) &= W(m,n)X(m,n)\ given\ W(m,n) \\ &= [W_R(m,n)\ W_G(m,n)\ W_B(m,n)]^T\ and\ X(m,n) \\ &= \{X_R(m,n), X_G(m,n), X_B(m,n)\} \end{aligned} \quad (3)$$

In (2) and (3), 'X_R', 'X_G', and 'X_B' represent pixel intensity matrices of the red, green, and blue color channels of the input color image 'X'. The notion '(m, n)' represents the vector of weight values used in the linear combination in (2). The values in the weight matrices

'$W_R(m, n)$', '$W_G(m, n)$', and '$W_B(m, n)$' at each pixel location are selected such that the intensity information and gradient information in the input color image are efficiently transferred to the output grayscale image 'Y' without significant loss during the decolorization process. In the context of the decolorization of macroscopic skin images, both intensity and edge information are highly relevant to ensure accurate segmentation of the lesions. It is hypothesized that upon efficient transfer of intensity information [17] from color space representation to grayscale space, the squared error between the Lightness (L) component of L*a*b* color space representation of the input image and the output grayscale image 'Y' will be minimized. Thus, the local value of the squared intensity error is,

$$E_L = [(m, n) - (m, n)]^2 \tag{4}$$

Another hypothecation is adopted such that upon efficient transfer of edge information from colour space representation to grey scale space, the squared error between the resultant local gradient computed from the L*a*b* colour space representation of the input image '∇_X(m, n)' and the gradient '$\nabla_Y(m, n)$' of the output grayscale image 'Y' will be minimum. Local value of the squared gradient error is, [8]

$$E\nabla(m, n) = [\nabla_X(\mathrm{m}, \mathrm{n}) - \nabla_Y(m, n)]^2 \tag{5}$$

The gradients computed from the lightness component 'L' and two colour dimensions (a and b) are used to compute the resultant gradient of the input colour image '∇_X' in (5). Thus the local value of the resultant gradient at an arbitrary pixel location '(m, n)' in the input colour image 'X' is,

$$\nabla_X(m, n) = \sqrt[3]{\nabla_L(m, n) + \nabla_a(m, n) + \nabla_b(m, n)} \tag{6}$$

In (6), the terms '∇_L(m, n)', '∇_a(m, n)', and '∇_b(m, n)' are the local gradient values in the L, a and b components of the L*a*b* colour space.

A cost function that collectively accounts for the efficiency of transferring the intensity and gradient information in the input colour image to the output grayscale. Space is constructed by combining the squared intensity error in (4) and squared gradient error in (6) as

$$E(m, n) = \alpha E_L + (1 - \alpha)E_\nabla, 0 \le \alpha \le 1 \tag{7}$$

In (7), the local value of the cost function '(m, n)' is a linear combination of local values of the squared intensity error [13,14]'$EL(m, n)$' and squared gradient error '$E\nabla(m, n)$'. The variable 'α' is a user-defined parameter that decides the relative importance of the constraints incorporated in the cost function in (7). As the cost function is in the form of a linear combination, the parameter 'α' is termed as Linear Combination Coefficient (LCC). As per (2) to (7), the local value of the cost function '$E(m, n)$' is a function of the local pixel value in output grayscale image '$Y(m, n)$' and the local pixel value in the decolourized image is a function of the weights '$W_R(m, n)$', '$W_G(m, n)$' and '$W_B(m, n)$'. The combination of the weights that minimizes the local value of the cost function is optimal [15] as given in (8).

$$W_{Opt}(m, n) = \underset{\{W_R(m,n), W_G(m,n), W_B(m,n)\}}{argmin} [E(m, n)] \tag{8}$$

Optimum values of the local weights '(m, n)', '(m, n)' and '$W_B(m, n)$' are computed via a recursive search procedure. The prior decolourized image is initialized as,

$$Y_{t=0}(m,n) = \frac{1}{3}[X_R(m,n) + X_G(m,n) + X_B(m,n)] \quad (9)$$

The grey scale values in the prior are updated with those computed from the optimum combination of the weights that minimizes the cost function. The updating is repeated recursively until the error between the decolourized images at two consecutive recursions 'Y_t' and 'Y_{t-1}' is less than a user-defined threshold 'τ'. The error between the decolorized images at two consecutive recursions is [12,16].

$$e_t = \sum_{m=1}^{M}\sum_{n=1}^{N}|Y_t(m,n) - Y_{t-1}(m,n)|, t = 1,2,\dots\dots,T \quad (10)$$

In (10), 'T' is the maximum permitted number of recursions. In the present form of the ALCCD, the values of the threshold 'τ' and maximum permitted number of recursions 'T' respectively are $1/MN$ and 100.

A SCHEMATIC FLOW DIAGRAM IS REPRESENTED AS BELOW

Pseudo-code of ALCCD

Step 1: Convert the input colour image 'X' into the L*a*b* colour space

Step 2: Initialize the prior decolourized image 'Yt=0' using (9)

Step 3: Select/input the values of the user-defined parameters 'α', 'τ' and 'T'

Step 4: Calculate the cost function '(m, n)' at m=1 and n=1 using (4) to (7)

Step 5: Identify the optimum weight vector '(m, n)' following the constraint in (8)

Step 6: Replace the pixel value 'Y_t=0(m, n), at m = 1 and n = 1' with updated grey scale value calculated from the optimum weight vector '$W_{Opt}(m, n)$' using (2).

Step 7: Update the grey scale values 'Yt=0(m, n), at m = 2,3 … … , M and n = 2,3 … … , N' repeating step 4 to step 6.

Step 8: Calculate the error 'et' between the decolourized images at two consecutive recursions 'Y_t' and 'Y_{t-1}'

Step 9: Repeat the step 4 to step 8 if $et \leq \tau$

5. Results and Discussion

5.1 Subjective Evaluation of the Performance of the ALCCD and Comparison with Existing Decolourization Algorithms

The perceptual quality of the grayscale images produced by the ALCCD is assessed here and compared against existing decolorization algorithms. Existing decolorization algorithms in the literature are CD (Nafchi etal. 2017), DVM (Jin etal. 2014), FCED (Grundland & Dodgson 2007), SD (Liu etal. 2017), GCSD (Liu etal. 2015), and LED (Liu etal. 2017). Three test images (Figure 1.1(a), Figure 1.2(a), and Figure 1.3(a)) with completely diverse lesion and background colors are selected to justify the performance of the ALCCD. Three representative macroscopic images [16] (Figure 1.1(a), Figure 1.2(a), and Figure 1.3(a))

of the skin lesions and corresponding decolorization outputs of CD, DVM, FCED, SD, GCSD, LED, and ALCCD are shown in Figures 1.1, 1.2, and 1.3.

In Figure 1, for test image 1 (Figure 1(a)), the background region in the output images of CD (Figure 1.1(b)), DVM (Figure 1(c)), FCED (Figure 1(d)), SD (Figure 1(e)), GCSD (Figure 1(f)), and LED (Figure 1(g)) seems to be enhanced and relatively brighter. The over-enhancement of the background region is dominantly visible in the output image of FCED in Figure 1(d). The surface of the output image of the FCED (Figure 1(d)) looks smooth, and textural information is lost. The over-enhancement of the background regions and loss of textural information are also evident in the output images of the FCED in Figure 2(d) and Figure 3(d), for test image 2 (Figure 2(a)) and test image 3 (Figure 3(a)). In test image 2 (Figure 2(a)), the lesion looks uncontrollably blurred in the output image of the FCED, as seen in Figure 2(d). For test image 2 (Figure 2(a)), a mild blurring effect on the lesion can be observed in the output images of CD (Figure 2(b)), SD (Figure 2(e)), and LED (Figure 2(g)). In test images 2 (Figure 2(a)) and 3 (Figure 3(a)), the DVM over-emphasizes the textural information, as seen in Figure 2(c) and Figure 3(c). In test image 3, the background region of the grayscale images produced by GCSD (Figure 3(f)) and LED (Figure 3(g)) also seems to be enhanced and relatively brighter. In the decolorized images produced by the ALCCD (Figure 1(h), Figure 2(h), and Figure 3(h)), over-emphasized texture or over-enhanced background illumination are not visible. The ALCCD does not over-emphasize texture or over-enhance background illumination. In terms of the similarity of the perceptual information among the color images and grayscale images obtained via decolorization, the ALCCD is superior to CD, DVM, FCED, SD, GCSD, and LED. The performance of the ALCCD is verified and compared against CD, DVM, FCED, SD, GCSD, and LED on all 137 test images.

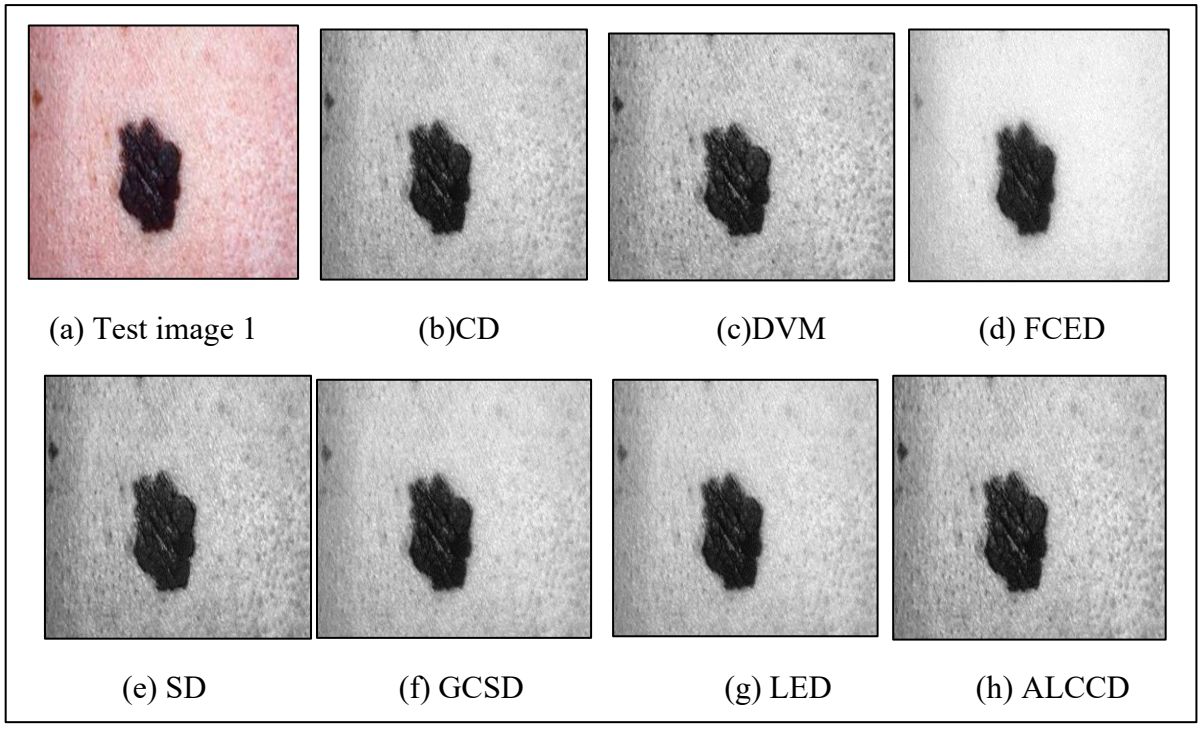

Figure 1. Decolourization Outputs of Various Algorithms on Test Image 1 (a) Test Image 1 (b) CD (c) DVM (d) FCED (e) SD (f) GCSD (g) LED (h) ALCCD

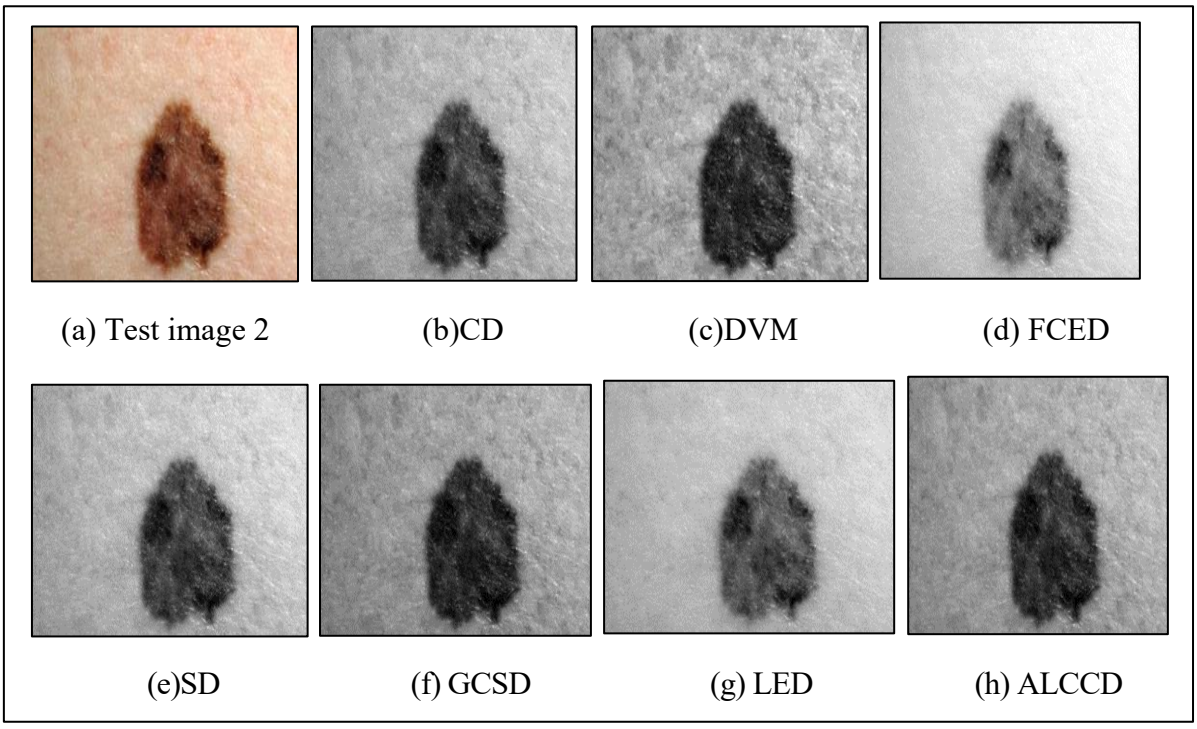

Figure 2. Decolourization Outputs of Various Algorithms on Test Image 2 (a) Test Image 2 (b) CD (c) DVM (d) FCED (e) SD (f) GCSD (g) LED (h) ALCCD

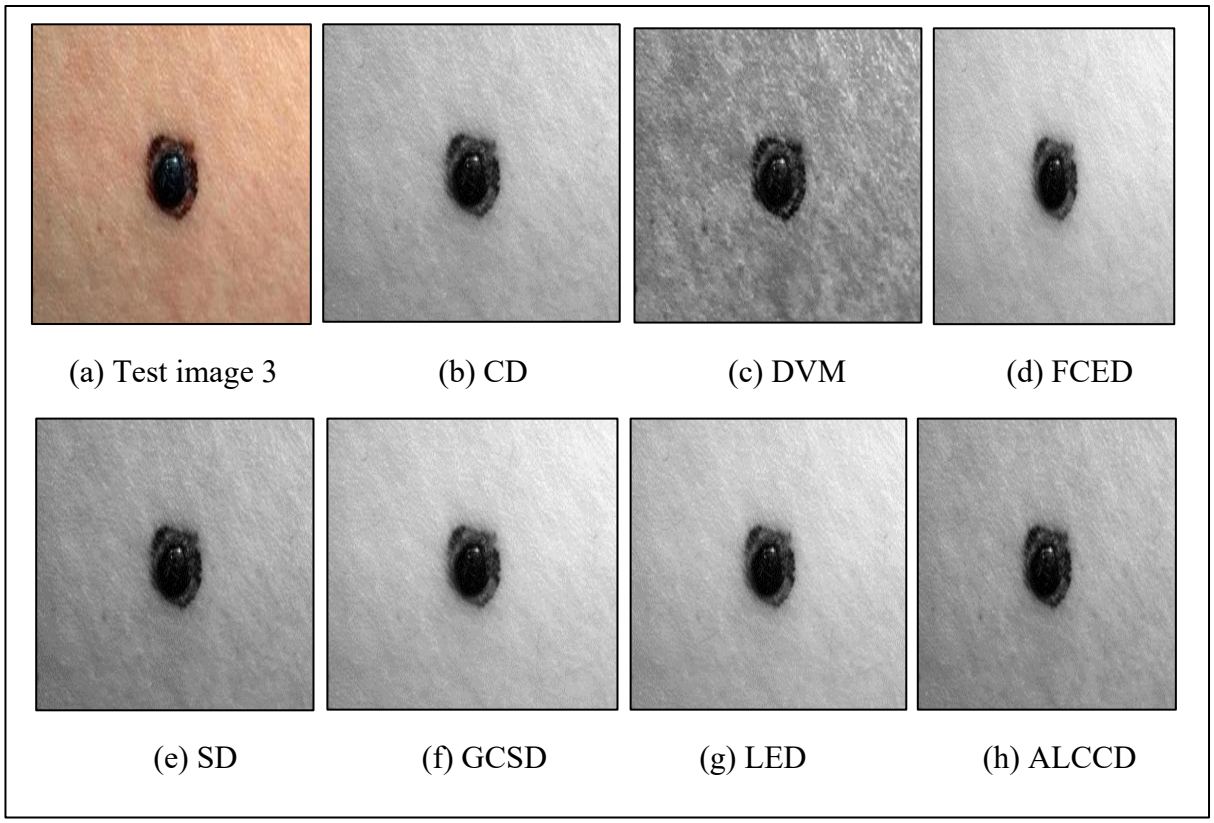

Figure 3. Decolourization Outputs of Various Algorithms on Test Image 3 (a) Test Image 2 (b) CD (c) DVM (d) FCED (e) SD (f) GCSD (g) LED (h) ALCCD

5.2 Task-based Performance Assessment of the ALCCD and Comparison with Existing Decolourization Algorithms

The existing decolorization algorithms CD, DVM, FCED, SD, GCSD, and LED focus only on the preservation of local contrast or gradient magnitude. Such algorithms may not ensure good accuracy of lesion segmentation on macroscopic images when intensity-based schemes are adopted. The segmentation results of Otsu's thresholding on the output images of CD, DVM, FCED, SD, GCSD, LED, and ALCCD produced from three test images (Figure 1(a), Figure 2(a), and Figure 3(a)) are shown in Figures 4, 5, and 6. Compared to the manual gold standard segmentations in Figures 4(a), 5(a), and 6(a), Otsu's thresholding has falsely segmented a significant portion of the background in the output images of CD (Figures 4(b), 5(b), and 6(b)), FCED (Figures 4(d), 5(d), and 6(d)), SD (Figures 4(e), 5(e), and 6(e)), GCSD (Figures 4(f), 5(f), and 6(f)), and LED (Figures 4(g), 5(g), and 6(g)). Otsu's thresholding produces segmentation results on the output images of ALCCD (Figures 4(h), 5(h), and 6(h)) that match the manual gold standard segmentations in Figures 4(a), 5(a), and 6(a) better than the segmentation results on the output images of CD, DVM, FCED, SD, GCSD, and LED. The ALCCD facilitates accurate segmentation of lesions on macroscopic images.

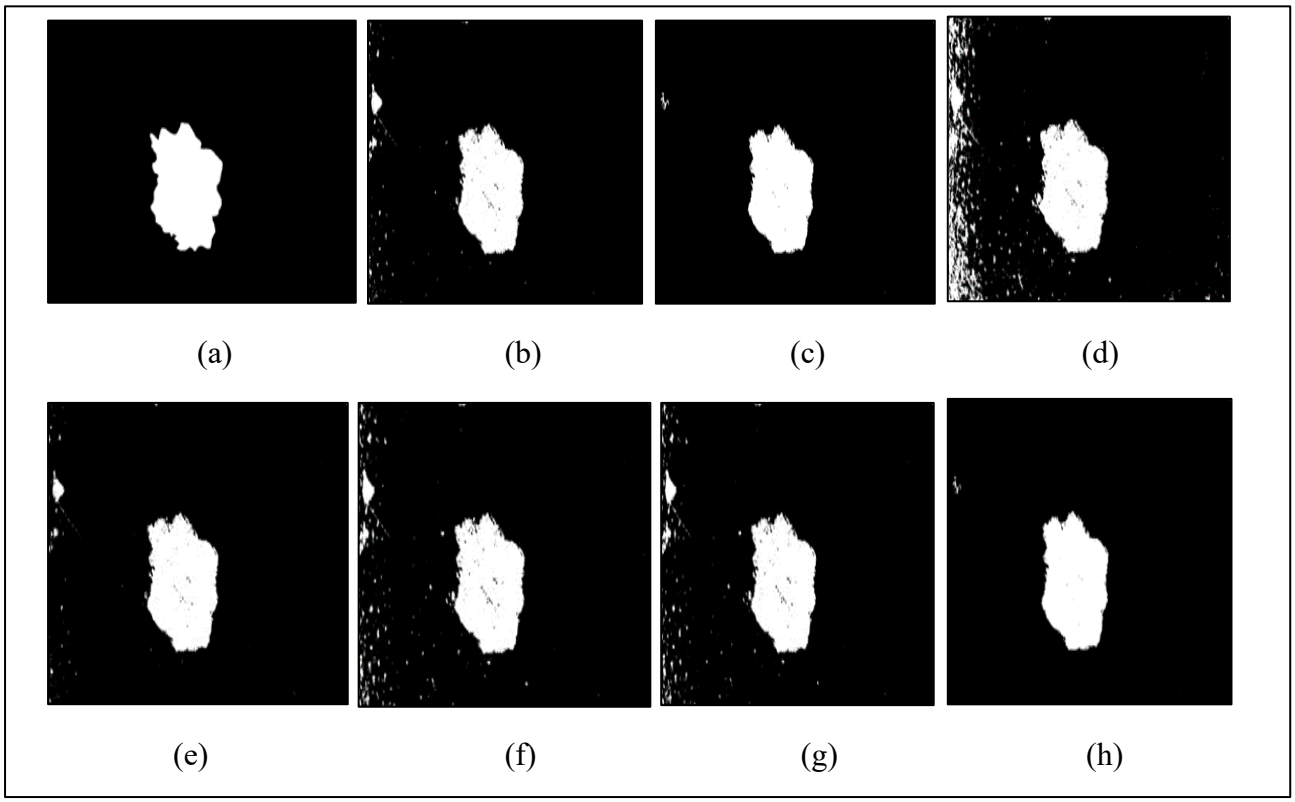

Figure 4. Segmentation Results of Otsu's Thresholding on the Output Images of Various Decolourization Algorithms Produced from the Test Image 1 (a) Manual Gold Standard Segmentation (b) CD (c) DVM (d) FCED (e) SD (f) GCSD (g) LED (h) ALCCD

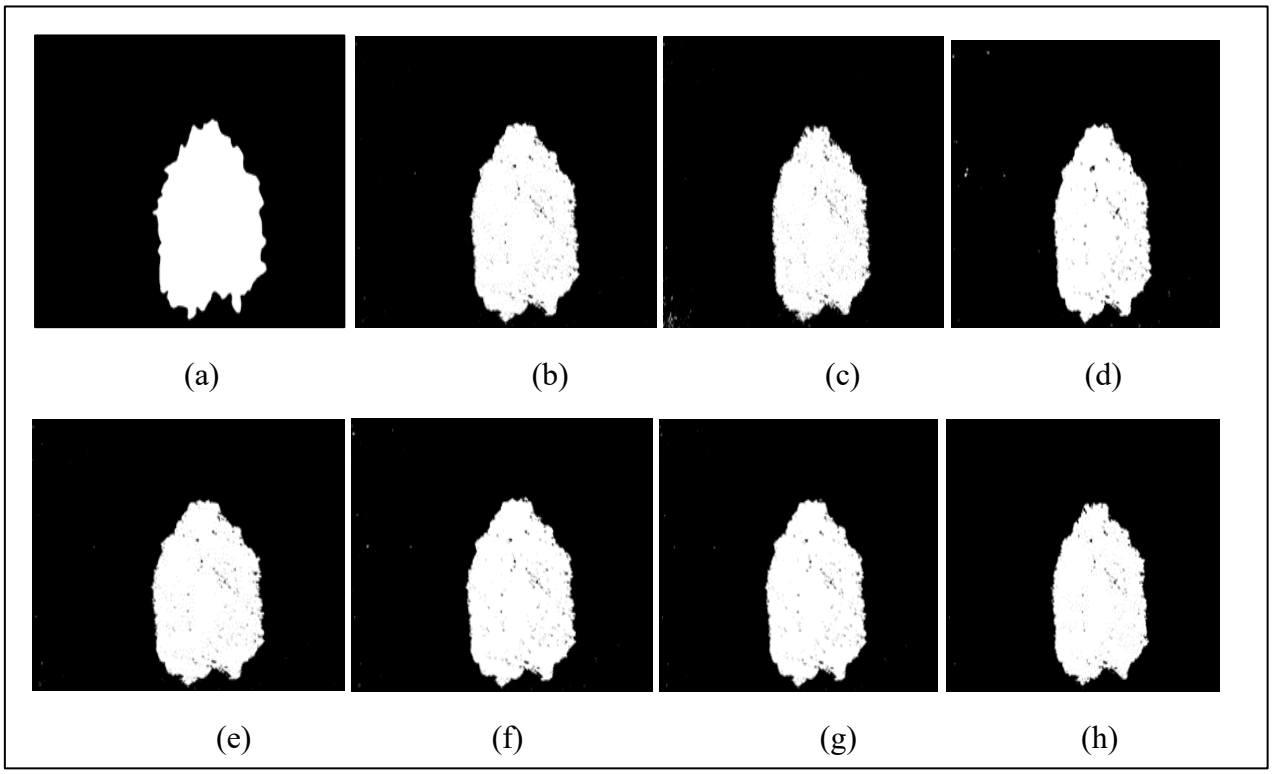

Figure 5. Segmentation Results of Otsu's Thresholding on the Output Images of Various Decolourization Algorithms Produced from the Test Image 2 (a) Manual Gold Standard Segmentation (b) CD (c) DVM (d) FCED (e) SD (f) GCSD (g) LED (h) ALCCD

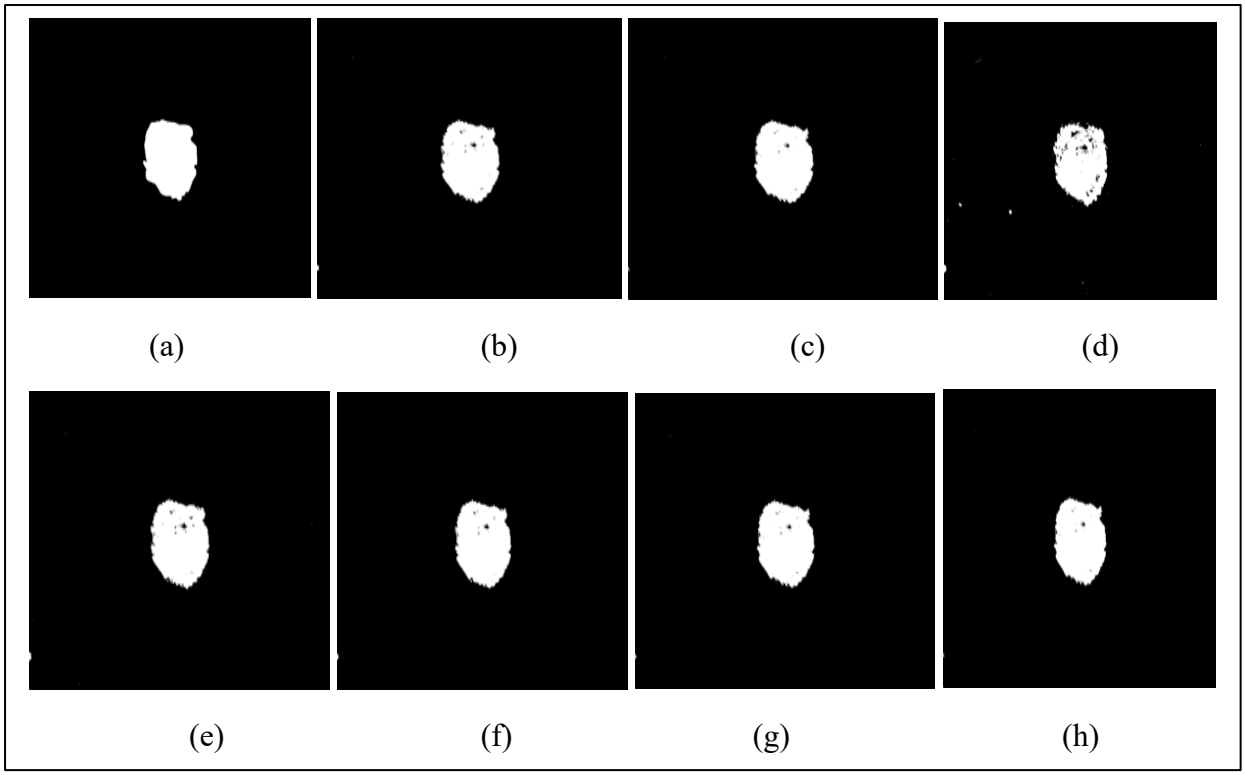

Figure 6. Segmentation Results of Otsu's Thresholding on the Output Images of Various Decolourization Algorithms Produced from the Test Image 3 (a) Manual Gold Standard Segmentation (b) CD (c) DVM (d) FCED (e) SD (f) GCSD (g) LED (h) ALCCD

The DSC values obtained from Otsu's segmentation on the output images CD, DVM, FCED, SD, GCSD, LED, and ALCCD are shown in Table 1. A bar graph of the average DSC obtained from the segmentation results of Otsu's thresholding on the output images of these decolourization algorithms on the entire dataset is shown in Figure 7. From Table 1, and Figure 7, it can be noted that Otsu's thresholding yields higher values of DSC on the output images of the ALCCD than on the CD, DVM, FCED, SD, GCSD, and LED.

Table 1. DSC values Obtained from Otsu's Segmentation on Output Images of Various Decolourization Techniques

Method	Test Image 1	Test Image 2	Test Image 3	Summary on entire dataset (Mean ± Std)
CD	0.9268	0.9535	0.9540	0.9455 ± 0.0162
DVM	0.9634	0.9542	0.9572	0.9570 ± 0.0071
FCED	0.7478	0.9493	0.9271	0.8752 ± 0.1110
SD	0.9392	0.9541	0.9554	0.9479 ± 0.0077
GCSD	0.8854	0.9508	0.9483	0.9321 ± 0.0405
LED	0.8977	0.9525	0.9503	0.9364 ± 0.0336
ALCCD	0.9647	0.9556	0.9583	0.9595 ± 0.0047

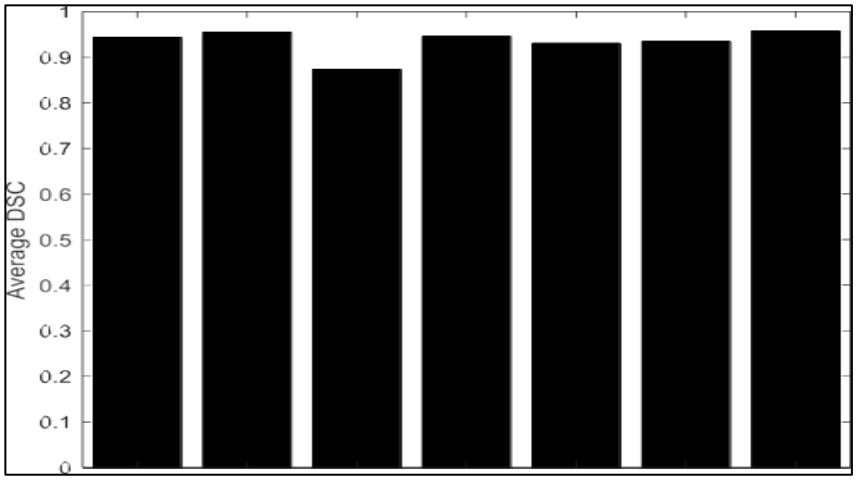

Figure 7. Bar Graph of the Average DSC Obtained from the Segmentation Results of Otsu's Thresholding on the Output Images of Various Decolourization Algorithms on the Entire Dataset

5.3 Selection of LCC

The ALCCD has an operational parameter that significantly impacts the quality of the decolorized images and, consequently, the accuracy of segmentation of the lesions when automated algorithms are employed for the task. Hence, a judicious choice of the LCC is

important to ensure good quality of the decolorized images produced by the ALCCD and better segmentation accuracy of the lesions. Considerations that drive the selection of the LCC are discussed here. The DSC versus LCC plots on three test images (Figure 1(a), Figure 2(a), and Figure 3(a)) are shown in Figure 8, Figure 9, and Figure 10. It can be seen that at an LCC value of 0.65, the DSC values are appreciably maximum. The LCC value of 0.65 is verified to be suitable for all 137 test images.

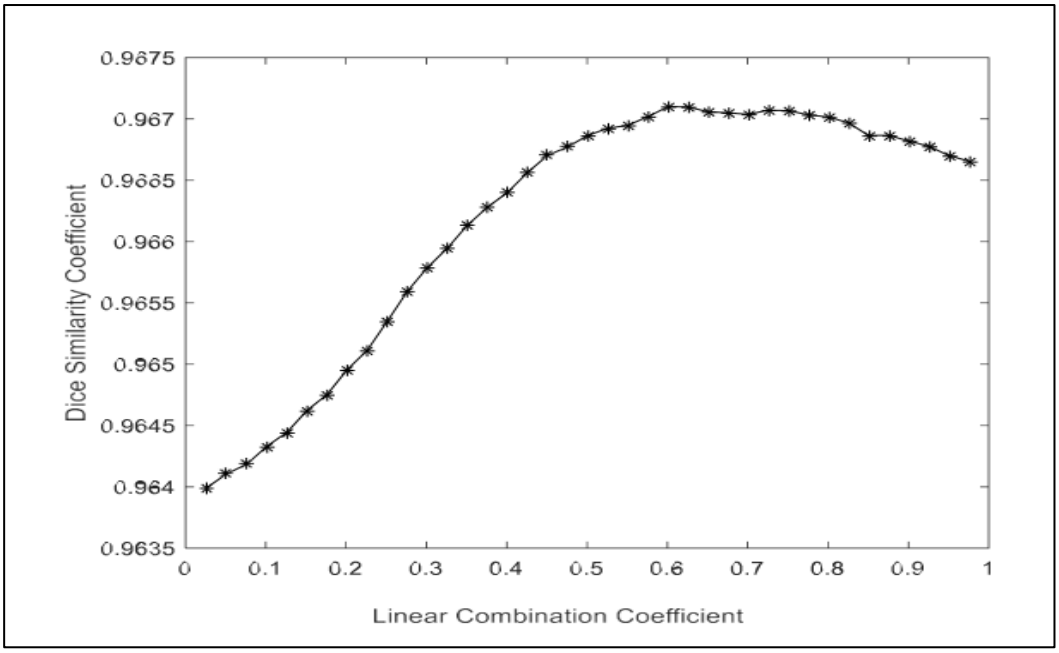

Figure 8. DSC versus LCC Plot on Test Image 1

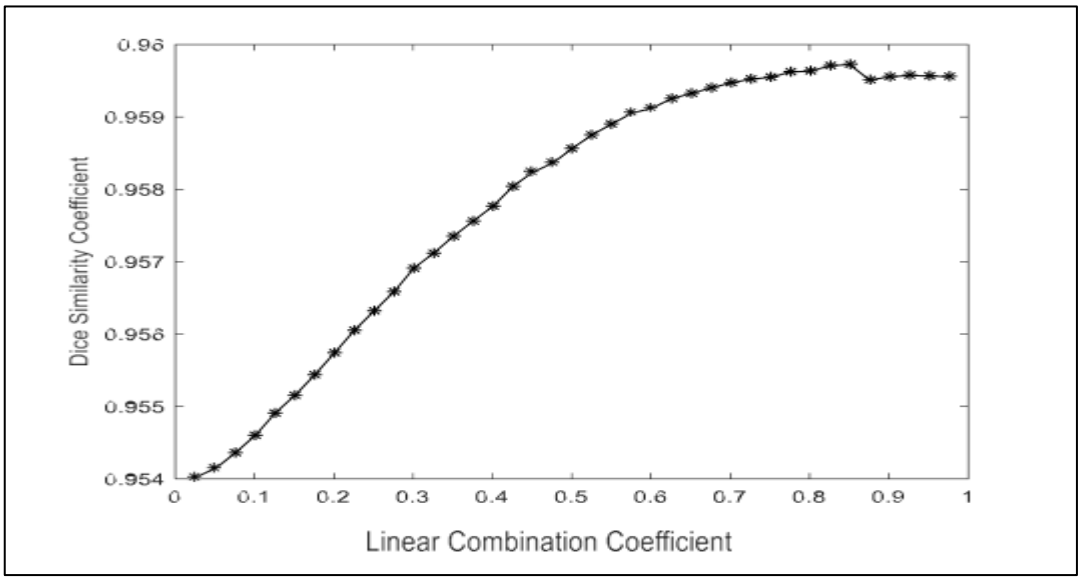

Figure 9. DSC versus LCC Plot on Test Image 2

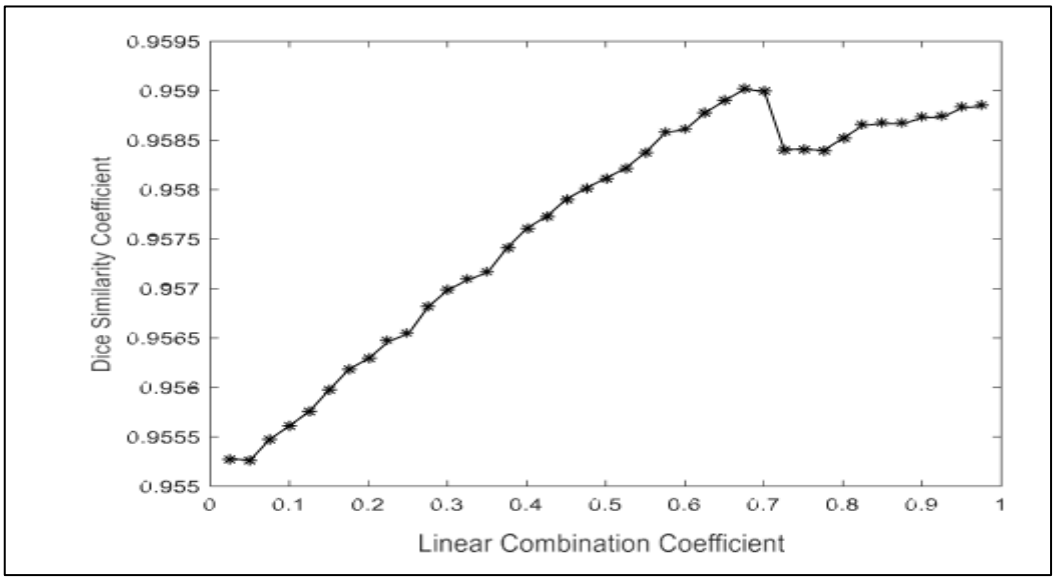

Figure 10. DSC versus LCC Plot on Test Image 3

6. Discussions

A decolourization algorithm named Adaptive Linear Combination-based Contrast-preserving Decolourization (ALCCD) preserves the contrast between the background skin regions and lesions when mapped from colour space to grayscale space and ensures accurate segmentation. Table 1.1 also shows 95% confidence intervals to indicate that the results are statistically strong. The value of the method is 0.9595 ± 0.0047 for the whole dataset. The ALCCD does not over-emphasize texture or over-enhance background illumination. In terms of the similarity of the perceptual information among the colour images and grayscale images obtained via decolourization, the ALCCD is superior to CD, DVM, FCED, SD, GCSD, and LED. Otsu's thresholding produces segmentation results on the output images of the ALCCD that match the manual gold standard segmentations better than the segmentation results on the output images of CD, DVM, FCED, SD, GCSD, and LED. Otsu's thresholding yields higher values of DSC on the output images of the ALCCD than on CD, DVM, FCED, SD, GCSD, and LED. The ALCCD facilitates accurate segmentation of lesions on macroscopic images. In its current form, the operational parameter LCC of the ALCCD is set manually. By using an image quality metric that measures the quality of decolourized images as a loss function, the selection of the LCC can be automated with the help of nature-inspired optimization algorithms as a future modification of the ALCCD.

7. Conclusion

The ALCCD does not overemphasize texture or over-enhance background illumination. In terms of the similarity of the perceptual information among the color images and grayscale images obtained via decolorization, the ALCCD is superior to CD, DVM, FCED, SD, GCSD, and LED. Otsu's thresholding produces segmentation results on the output images of the ALCCD that match the manual gold standard segmentations better than the segmentation results on the output images of CD, DVM, FCED, SD, GCSD, and LED.

References

[1] S. Sathish. M. G. Sumithra, K. Mohanasundaram," Shading and texture constrained for correcting vignetting on dermatologicalmacro images- The Visual Computer (SCI Indexed). https://doi.org/10.1007/s00371-021-02368-z

[2] MacLellan, AN, Price, EL, Brouwer, PB, Matheson, K, Ly, TY, Pasternak, S, NM, Walsh, Gallant, CJ, Oakley, A, Hull, PR & Langley, RG 2021, 'The use of non-invasive imaging techniques in the diagnosis of melanoma: a prospective diagnostic accuracy study', Journal of the American Academy of Dermatology, vol. 85, issue. 2: 353-359.

[3] Birkenfeld, JS, Tucker-Schwartz, JM, Soenksen, LR, Avilés-Izquierdo, JA & Marti-Fuster, B 2020, 'Computer-aided classification of suspicious pigmented lesions using wide-field images', Computer Methods and Programs in Biomedicine, vol. 195: 105631

[4] Amelard, R, Glaister, J, Wong, A & Clausi, DA 2015, 'High-level intuitive features (HLIFs) for intuitive skin lesion description', IEEE Transactions on Biomedical Engineering, vol. 62, no. 3: 820-831.

[5] Saleem, A, Bhatti, N, Ashraf, A, Zia, M & Mehmood, H 2019, 'Segmentation and classification of consumer-grade and dermoscopic skin cancer images using hybrid textural analysis', Journal of medical imaging, vol. 6, issue 3, 034501

[6] Pereira, PMM, Fonseca-Pinto, R, Paiva, RP, Assuncao, PAA, Tavora, LMN, Thomaz, LA & Faria, SMM 2020, 'Dermoscopic skin lesion image segmentation based on local binary pattern clustering: a comparative study', Biomedical Signal Processing, and Control, vol. 59, 101924.

[7] DermQuest. 2021, https://uwaterloo.ca/vision-image-processing-lab/research-demos/skin-cancer-detection

[8] Gautam, D, Ahmed, M, Meena, YK & Ul Haq, A 2018, 'Machine learning-based diagnosis of melanoma using macro images' International Journal of Numerical Methods in Biomedical Engineering, vol. 34: e2953.

[9] Jaisakthi, SM, Mirunalini, P & Aravindan, C 2018, 'Automated skin lesion segmentation of dermoscopic images using GrabCut and k-means algorithms', IET Computer Vision, vol. 12, issue 8: 1088-1095

[10] Lee, H & Chen, YPP 2014, 'Skin cancer extraction with optimum fuzzy thresholding technique', Applied Intelligence, vol. 40, pp. 415-426, https://doi.org/10.1007/s10489-013-0474-0

[11] Liu, Q, Liu, PX, Xie, W, Wang, Y & Liang, D 2015, 'GcsDecolor: gradient correlation similarity for efficient contrast preserving decolorization', IEEE Transactions on Image Processing, vol. 24, no. 9: 2889-2904

[12] M.Neela Harish ,padmasini V , Prathiba Palaniappan "Study of the Movements of Active Upper Limb Prostheses" . https://ieeexplore.ieee.org/document/10940104

[13] Durai Arumugam, S. S. L., & Praveen Kumar, R. (2024). Hybrid Optimized Gated Recurrent Unit with Ridge Classifier for Crop Recommendation for Precise Agriculture

Using Fused Feature Selection Concept. International Journal on Artificial Intelligence Tools, 33(04), 2450012.

[14] Sathish S, K. Yamuna Devi a, J. Shanmuga Priyan b , P.G. Kuppusamy , Deepa Beeta Thiyam d , Vipin Venugopal, Probabilistic luminance estimation and optimized gamma correction for Wireless capsule endoscopy, https://doi.org/10.1016/j.bspc.2025.1075

[15] SSL, D. A., & Kumar, P. (2024). Serial cascaded deep feature extraction-based adaptive attention dilated model for crop recommendation framework. Applied Soft Computing, 162, 111790.

[16] Raja S, K. S. (2024). HHECC-AES: A Novel Hybrid Cryptography Scheme for Developing the Secured Wireless Body Area Network Using Heuristic-aided Blockchain Model. Adhoc & Sensor Wireless Networks, 59.

[17] Assessment of Gamma Band Power of Electroencephalogram in Alzheimer's disease Vinurajkumar S, Yamuna Devi K, Manikandan K, Sathish S DOI: 10.1080/23279095.2025.2540586.